Available online at www.sciencedirect.com

SciVerse ScienceDirect

journal homepage: www.elsevier.com/locate/he

Thermal analysis of air-cooled PEM fuel cells

Setareh Shahsavari [a], Andrew Desouza [b], Majid Bahrami [a], Erik Kjeang [a,*]

[a] Mechatronic Systems Engineering, School of Engineering Science, Simon Fraser University, 250-13450 102 Avenue, Surrey, BC V3T 0A3 Canada

[b] Ballard Power Systems, Inc., 9000 Glenlyon Parkway, Burnaby, BC V5J 5J8 Canada

ARTICLE INFO

Article history:
Received 10 July 2012
Received in revised form
7 September 2012
Accepted 11 September 2012
Available online 11 October 2012

Keywords:
PEM fuel cell
Air cooling
Thermal management
Forced convection
Heat transfer
Numerical modeling

ABSTRACT

Air-cooled proton exchange membrane fuel cells (PEMFCs), having combined air cooling and oxidant supply channels, offer significantly reduced bill of materials and system complexity compared to conventional, water-cooled fuel cells. Thermal management of air-cooled fuel cells is however a major challenge. In the present study, a 3D numerical thermal model is presented to analyze the heat transfer and predict the temperature distribution in air-cooled PEMFCs. Conservation equations of mass, momentum, species, and energy are solved in the oxidant channel, while energy equation is solved in the entire domain, including the membrane electrode assembly (MEA) and bipolar plates. The model is validated with experiments and can reasonably predict the maximum temperature and main temperature gradients in the stack. Large temperature variations are found between the cool incoming air flow and the hot bipolar plates and MEA, and in contrast to water-cooled fuel cells, significant temperature gradients are detected in the flow direction. Furthermore, the air velocity and in-plane thermal conductivity of the plate are found to play an important role in the thermal performance of the stack.

1. Introduction

Operation of a polymer electrolyte membrane fuel cell (PEMFC) is a complex process that includes electrochemical reactions coupled with transport of mass, momentum, energy, species and charges that occur on a wide range of length scales [1]. Different parts of a PEMFC are comprised of current collectors, anode and cathode flow channels, gas diffusion layers (GDLs), catalyst layers and membrane [2]. During operation of a PEMFC, hydrogen molecules are supplied at the anode and split into protons and electrons. The polymeric membrane conducts protons to the cathode while the electrons move from anode to cathode through an external load powered by the cell. Oxygen (from air) reacts with the protons and electrons in the cathode half-cell where water and heat are produced.

A simple way to improve the performance of a fuel cell is to operate the system at its maximum allowed temperature. At higher-temperature, electrochemical activities increase and reaction takes place at a higher rate, which in turn increases the power output. On the other hand, operating temperature affects the maximum theoretical voltage at which a fuel cell can operate. Higher temperature corresponds to lower theoretical maximum voltage and lower theoretical efficiency [3]. Temperature in the cell also influences cell humidity, which significantly influences membrane ionic conductivity. Therefore, temperature has an indirect effect on cell performance through its impact on the membrane water content. The

* Corresponding author. Tel.: +1 778 782 8791; fax: +1 778 782 7514.
E-mail address: ekjeang@sfu.ca (E. Kjeang).

0360-3199/$ – see front matter
http://dx.doi.org/10.1016/j.ijhydene.2012.09.075

durability of the membrane electrolyte is another barrier for higher-temperature operation due to performance degradation during long-term operation. As a result, the operating temperature is selected by considering the durability of the membrane electrolyte. The main purpose of thermal management in fuel cell systems is to ensure stack operation within a reliable temperature range and to provide a more uniform temperature distribution in the stack. A detailed understanding of the stack thermal behavior is therefore necessary for design and development of an efficient cooling solution. Oosterkamp [4] addressed some of the heat transfer issues for both PEM based systems and solid oxide fuel cell (SOFC) systems.

Many studies are available on analytical and numerical modeling of PEMFCs [5–16] and several researchers have concentrated on the area of thermal modeling and thermal management [17–26]. Chupin et al. [20] presented a one-dimensional thermal model for a water-cooled fuel cell. Promislow and Wetton [21] decoupled the cross-plane heat transfer at each channel and presented a one-dimensional thermal model that determines the temperature distribution through a unit fuel cell with straight flow channels. Shan and Choe [22] also considered a one-dimensional temperature gradient across the fuel cell stack in the through-plane direction, assuming that the temperature is constant at each cell but varies from cell to cell. Yu and Jung [23] developed a two-dimensional numerical thermal model of a water-cooled PEMFC. The heat transfer sub-model included the conduction heat transfer inside the MEA and convective heat rejection from MEA to cooling water flow and gases. Pharoah and Burheim [24] presented a two-dimensional thermal model and obtained temperature distributions in a PEMFC in the plane normal to the cathode flow direction. In this case, convective heat transfer was neglected. Sasmito et al. [27] developed a two-dimensional numerical model to investigate the forced-air convection heat transfer in a small, open-cathode air-cooled PEMFC and studied the effects of the fan power and pressure drop on the overall performance. A three-dimensional model was developed by Shimpalee and Dutta [17], which solved the energy equation to predict the temperature distribution inside a straight channel PEMFC. Adzakpa et al. [25] developed a three-dimensional dynamic model of a single cell and included the thermal conduction and heat generation inside the fuel cell without considering internal convective heat transfer. A three-dimensional model that included analysis of species, heat, and charge transport in a single-channel unit cell, was presented by Sinha and Wang [26]. They investigated the performance of a PEMFC operating at high temperature. In their thermal model, a constant temperature condition was applied on all the external boundaries of the fuel cell. Ramousse et al. [28] analyzed electrochemical performances as a function of the temperature distribution. In their thermal model they neglected convective heat transfer inside the stack [28]. The system-level thermal management of PEMFC stacks is also studied. A simple description of thermal effects at the system-level is given in Ref. [29].

The majority of the PEMFC thermal studies published to date apply to either a single fuel cell without a cooling system or water-cooled fuel cell stacks. Thermal analysis of air-cooled fuel cells has not been considered extensively in the literature. Air-cooled fuel cell systems combine the cooling function with the cathode flow field and reduce the overall cost by (i) eliminating many of the auxiliary systems required for conventional fuel cell designs (water cooling loop, air compressor, and humidifier) and (ii) enabling a single bipolar fuel cell plate design. The main applications of the air-cooled fuel cell are in portable and backup power generation. Our present objective is to develop a three-dimensional thermal model of an air-cooled PEMFC stack in order to predict temperature distribution and heat transfer coefficients and perform parametric studies to investigate thermal management strategies. The results of the modeling activities are validated by experimental data collected by our industrial partner, Ballard Power Systems, Inc. Parametric studies include investigating the effects of air velocity and bipolar plate and gas diffusion layer (GDL) in-plane and through-plane thermal conductivities on the stack temperature.

2. Model description

One of the most challenging aspects of computational modeling of PEMFCs is the multi-physics and multi-scale nature of the transport processes, and the coupling between different processes and length scales [30]. The development of a complete three-dimensional PEMFC model that considers all the components with simultaneous transport phenomena is a complex and challenging task. Furthermore, if the entire fuel cell stack composed of several cells is considered as the computational domain, modeling multi-physics processes involves significant computational cost, even by using high performance advanced numerical algorithms and taking advantage of parallel computing. The present model aims to capture the main thermal characteristics of air-cooled PEMFC stacks at reasonable accuracy while reducing the computational cost. This can be done by decoupling the heat transfer mode from charge transport and by considering a computational domain that can feature the two most important stack-level thermal characteristics of air-cooled fuel cells: the maximum stack temperature, and the main temperature gradient which has been observed experimentally to occur in the flow direction.

2.1. *Computational domain*

Two computational domains are considered in the present study: (i) a complete cell with 80 cathode flow channels and (ii) a single cathode channel with plate and MEA surrounding it in the central cell. A cell-level model can represent the fuel cell stack behavior by using periodic boundary conditions. Since the computation time for a complete cell model is high, a channel-level model is considered for parametric studies. As explained previously, it is desirable to operate the fuel cell system at a temperature slightly below the maximum allowable temperature. The channel-level model captures the extreme temperature conditions by considering the central cathode channel, which experiences the maximum temperature in the entire stack. The computational domains corresponding to the cell-level and channel-level models are both illustrated in Fig. 1. Taking advantage of symmetry in the fuel

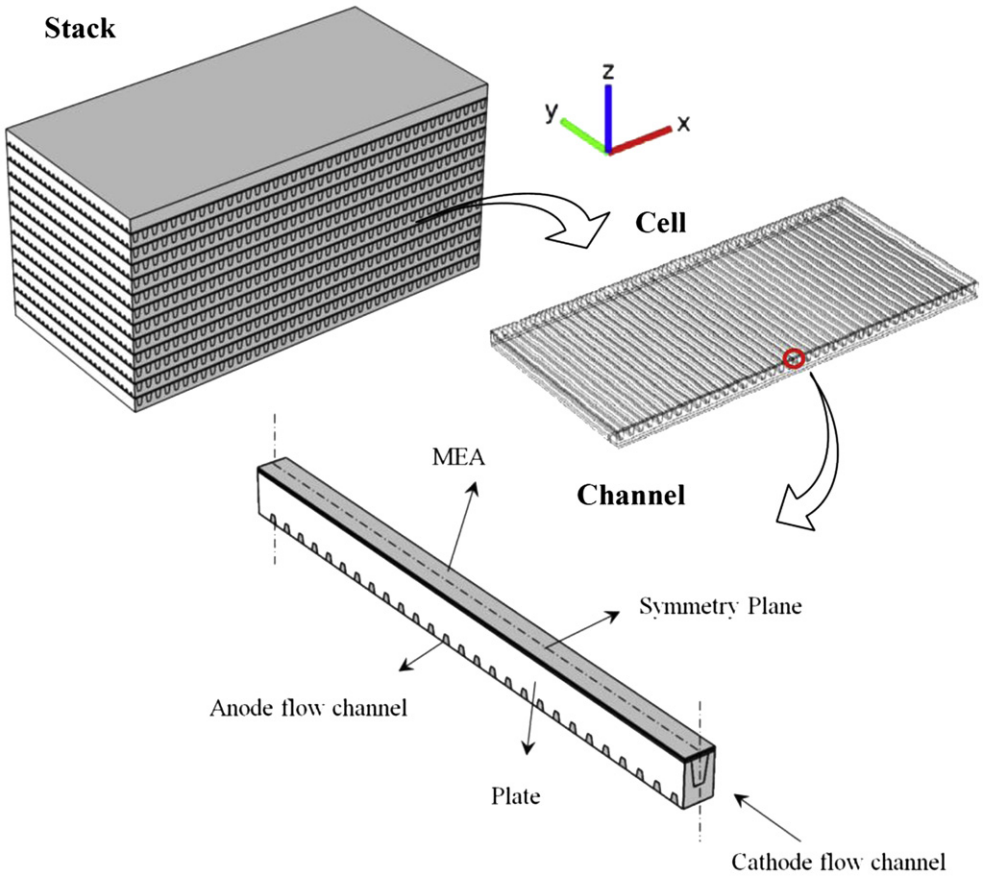

Fig. 1 – 3D schematic of an air-cooled fuel cell stack. The central cell and the central cathode channel are considered in the present model.

cell geometry, the equations are solved in half of the computational domain. Since air-cooled fuel cell stacks are the focus of this study, ambient air plenums are included at the inlet and outlet of the cell and channel, as shown in Fig. 2. These air plenums are required to adequately capture the sudden contraction and expansion of the flow entering and exiting the channel as well as the heat transfer from the end walls.

2.2. *Governing equations*

The present model considers heat transfer in the entire domain and laminar fluid flow and species transport in the oxidant channel and does not include the electrochemical reactions; local current density and cell voltage are inputs of the model. Since we have used the experimental values of these inputs, it is possible to obtain the temperature distribution both qualitatively and quantitatively. The experimental data for local current density (consisting of 96 data points on each cell) shows that the current density distribution is almost uniform in more than 90% of the cell area. The maximum gradient is seen at the bipolar plate edges, relatively far from the central cathode channel. Nevertheless, the small variation of current density in the central channel is included in the present model. The following main assumptions are made to model the fluid flow and heat transfer in an air-cooled PEMFC stack: (1) continuous, steady state, single phase laminar ($Re < 800$) incompressible flow ($Ma < 0.3$) is assumed; (2) convective heat transfer in anode channel and

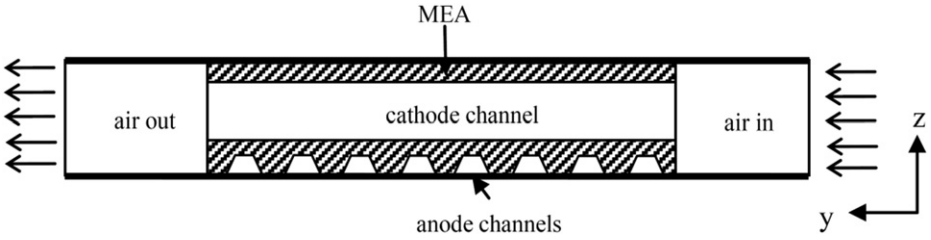

Fig. 2 – Cross-section of the computational domain including ambient air plenums at inlet (right) and outlet (left). The dark lines on top and bottom specify periodic boundary conditions.

GDL is neglected due to the relatively low velocity of fluid in these regions (anode channels are dead-ended); (3) constant thermophysical properties are assumed for the solid phase; (4) radiation heat transfer is neglected since the temperature is relatively low and the surface area of the domain exposed to radiation is small compared to the total surface area; and (5) heat generation is assumed to have a linear relationship with local current density.

For the solid region, the mechanism of heat transfer is conduction. The energy equation is as follows:

$$\nabla\cdot(k\nabla T)+\dot{q}=0 \tag{1}$$

where T is the temperature of the solid region. The term $\dot{q}$ is the source term for heat generation and is assumed to be zero except in the cathode catalyst layer, where the reaction heat is released. In order to determine the amount of heat produced by a fuel cell stack can be provided:

$$\sum_i H_{i,in}=\sum_i H_{i,out}+\dot{W}_{stack,gross}+\dot{Q}_{total} \tag{2}$$

where $H_{i,in}$ and $H_{i,out}$ are the enthalpies of reactants and products respectively. The heat generation calculated using Eq. (2) can be approximated by the following equation [12]:

$$\dot{Q}_{total}=(E-V_{cell})In_{cell} \tag{3}$$

where n_{cell} is the number of cells in a stack and E is the maximum voltage obtained if the hydrogen heating value or enthalpy of formation were transformed into electrical energy, and is given by [2]:

$$E=-\frac{\Delta H}{nF} \tag{4}$$

The enthalpy of formation of water vapor at 25 °C, 100 kPa is $-241{,}826$ kJ kmol^{-1}. Therefore, if the lower heating value (LHV) is used as ΔH in Eq. (4), E (25 °C) = 1.253 V. Due to the relatively low relative humidity and current densities of air-cooled fuel cells, the majority of the water produced is expected to remain in the vapor phase and the presence of liquid water is neglected. It should be noted that by using the LHV, the cooling effect of evaporation is implicitly included in the heat generation of Eq. (3). This equation also includes other sources of heat generation such as ohmic heating. In this study, V_{cell} and I are inputs of the model obtained from experimental measurements.

In the cell-level model, natural convection heat transfer is applied on the edges while in the channel-level model, symmetry boundary condition is applied on the side walls. The periodic heat transfer condition is applied on the top and bottom surfaces of the cell, where it contacts the adjacent cells in the stack. This boundary condition implies that T (at z_{min}) = T (at z_{max}) and also $\dot{q}_n$ (at z_{min}) = $\dot{q}_n$ (at z_{max}) (see axes in Figs. 1 and 2). In the cathode fluid region, due to the high stoichiometry of air (~100) the consumption of oxygen and production of water vapor do not affect the overall thermophysical properties and temperature distribution. Therefore,

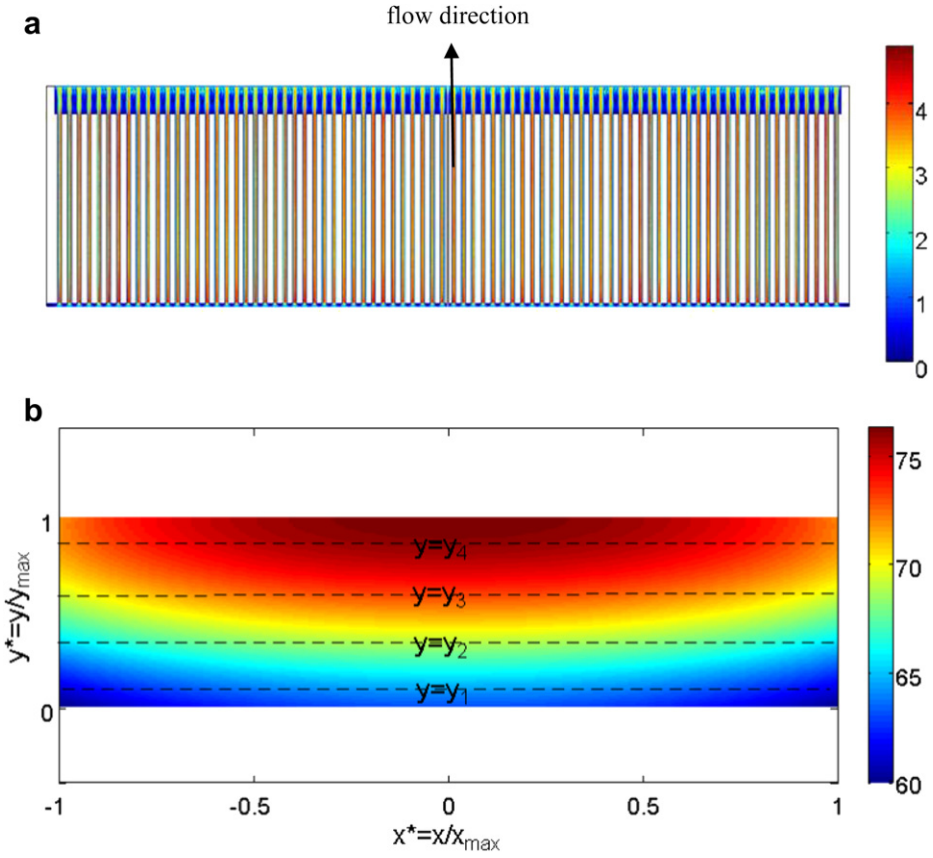

Fig. 3 – Cell-level model results for case 1: (a) air velocity magnitude [m s^{-1}]; and (b) temperature distribution in the bipolar plate [°C].

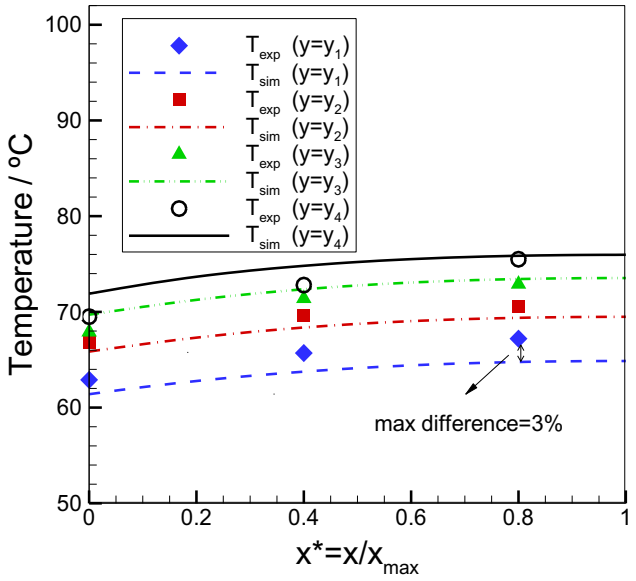

Fig. 4 – Comparison of plate temperature for case 1: cell-level model (lines) and measured data (symbols) at different locations for the central cell in the stack. Four lines, y_1, …, y_4, from oxidant inlet to outlet are specified in Fig. 3.

we have neglected the oxygen depletion and only considered water vapor generation to investigate the effect of temperature on relative humidity distribution inside the channel. Assuming continuous, steady state, laminar, incompressible flow inside the cathode channels and air plenums, the conservation equations of mass, species, momentum, and, energy are as follows:

$$\nabla\cdot(\rho\mathbf{u}) = S_{\text{mass}} \tag{5}$$

$$\mathbf{u}\cdot\nabla c = \nabla\cdot(D\nabla c) + S_{\text{mol}} \tag{6}$$

$$\rho\mathbf{u}\cdot\nabla\mathbf{u} = -\nabla p + \mu\nabla^2\mathbf{u} \tag{7}$$

$$\rho c_p\mathbf{u}\cdot\nabla T_f = \nabla\cdot(k\nabla T_f) \tag{8}$$

where $\mathbf{u}$ is the velocity vector (m s^{-1}), S_{mass} (kg m^{-3} s^{-1}) and S_{mol} (mol m^{-3} s^{-1}) are source terms for mass and species transport, respectively. Two species are considered in the fluid region: air and water vapor. The transport of water vapor in the air stream takes place through convection and diffusion. In Eq. (6), D denotes the binary diffusion coefficient of water vapor in air, which depends on temperature and can be described by the following relation proposed by Bolz and Tuve [31]:

$$D = -2.775\times10^{-6}\left[\frac{m^2}{s}\right] + 4.479\times10^{-8}\left[\frac{m^2}{s\,K}\right]T + 1.656 \times 10^{-10}\left[\frac{m^2}{s\,K^2}\right]T^2 \tag{9}$$

In the present model, the water vapor production is defined as a molar flux boundary condition at the interface of MEA and oxidant channel that accounts for the total species flux across the boundary. This implies that all the produced water is assumed to be removed through the oxidant channel. The rate of water vapor generation in the cathode half-cell is derived by:

$$\dot{m}_{H_2O,\text{produced}} = \frac{IM_{H_2O}}{2F} \tag{10}$$

Since the flow is continuous, no slip and no temperature jump conditions are applied at the wall. Therefore, the boundary condition for velocity field is u (at wall) = 0 and for temperature field is T (at wall) = T_{wall}. The flow enters with a constant uniform velocity, u_{in}, and constant temperature, T_{in}. For the fluid flow conditions at the outlet, no viscous stress along with constant atmospheric pressure, p_{atm}, are considered.

For the species transport equation, the boundary condition at the inlet is the ambient air relative humidity specified by a constant concentration: $c = c_{\text{in}}$. At the outlet, the species is transported out of the domain by the fluid flow. Here, convection is the dominating effect and the diffusive contribution can be ignored, such that:

$$\mathbf{n}\cdot(-D\nabla c) = 0 \tag{11}$$

For solving the system of partial differential equations described above, COMSOL Multiphysics 4.2a is used. Constant thermophysical properties are assumed for the solid phase while air properties such as density, heat capacity, dynamic viscosity, and thermal conductivity vary with temperature. Air density is obtained from the ideal gas law. Other thermophysical properties of air are obtained from COMSOL library.

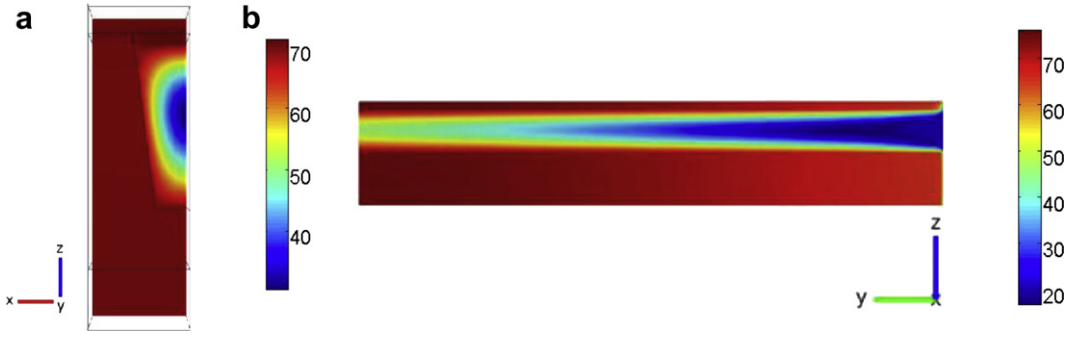

Fig. 5 – Channel-level model results for case 1: temperature profiles in the middle cross-section of the channel (a) normal and (b) parallel to the oxidant flow direction.

Table 1 – Model validation.

Case #	Air inlet velocity, u [m s^{-1}]	Cell heat generation, $\dot{Q}_{cell}$ [W]	Maximum temperature, T_{max} [°C]		Relative difference, $\frac{T_{sim}-T_{exp}}{T_{sim}}$
			Experiment[a]	Simulation	
1	1.76	55.7	76	77	1.3%
2	2.19	37.7	65	68	4.4%
3	1.63	27.6	61	64	4.7%
4	1.45	29.1	67	69	2.8%
5	0.95	6.3	35	36	2.7%
6	0.94	13.7	50	54	7.4%

a Experimental results from Ballard Power Systems.

Grid independency is checked by solving a case study using three different mesh sizes. For the channel-level study, three mesh sizes consisting of 3.5×10^5, 7.0×10^5, and 1.4×10^6 elements were implemented. We found that the mesh size of 7.0×10^5 elements gives approximately 1% deviation in terms of local temperature, velocities, and pressure compared to the finest mesh and therefore is sufficient for the numerical investigation purposes. For the cell-level model, a mesh size of 1.4×10^7 elements leads to a mesh-independent result. The computation time for the channel-level model is 30 min and for the cell-level simulation is 5 days on a PC with Intel Core2 2.66 GHz processor. Hence, the channel-level model is considered for the parametric studies.

3. Results and discussion

3.1. Model validation

To validate the model with experimental data and also to verify the practicality of the boundary conditions considered in the channel-level model, the three-dimensional numerical model described in Section 2 is first solved on the cell level. The cell-level simulation is conducted under the test conditions that generate the highest amount of heat in a Ballard air-cooled PEMFC stack. The velocity magnitude in the flow channels and the bipolar plate temperature distribution are presented in Fig. 3(a) and (b), respectively. The isothermal contours in Fig. 3(b) are flat in the central channels, which indicates that thermally insulated boundary condition can be considered in the channel-level model. The plate temperature is measured in the Ballard ACS stack at 24 different positions using thermocouples arranged in a 6×4 matrix: 6 points along x axis and 4 points along y axis. Fig. 4 compares these data points with simulated temperature variation in x-direction at four equivalent lines located at $y = y_1, \ldots, y_4$ (see Fig. 3), from cathode inlet to outlet. The difference between measured and predicted temperature is less than 3% for all points.

Similarly, for validating the channel-level model, simulations under certain conditions are performed and compared with experimental data. Fig. 5 shows the simulated temperature profiles in the middle cross-section of the channel in the normal (a) and parallel (b) directions to the flow. In the solid, a prominent gradient exists in the y direction parallel to the flow in the cathode channel, whereas relatively high temperature gradients exist in all directions in the flow channel.

The obtained maximum stack temperatures for different cases are presented in Table 1. The location of the maximum temperature as observed in the experiments is the plate temperature at the outlet of the central channel in the middle row of the stack, in agreement with the modeling approach. In the tests reported in Table 1, the inlet air temperature is constant at the room temperature, 21 °C, while the air velocity and the cell voltage vary in different cases. The operating conditions in case 1 (Table 1), are the same as for the cell-level simulation shown in Figs. 3 and 4. The last column in this table shows the relative difference between predicted maximum temperature and experimentally measured maximum temperature. Overall, the modeling results are within a few degrees of the measured data (the relative difference is in the range of 1–7%).

3.2. Reference case

To elucidate the overall thermal characteristics of air-cooled fuel cells and to perform parametric studies, a reference case is investigated in the single-channel level. In this reference case (described schematically in Figs. 1 and 2 and parametrically in Table 2), the inlet air velocity is selected to 3.0 m s^{-1}, the inlet air temperature is 20 °C, and the total heat generated in one cell is 48 W. Assuming 80 channels in one cell, the total heat generated in the modeling domain (half channel) is 0.3 W. The material thermophysical properties assumed for the reference case are listed in Table 2.

Table 2 – Geometrical and thermophysical parameters assumed in the reference case.

t_{BP}	5.50 mm	$t_{rib,cathode}$	1.50 mm
$t_{GDL,anode}$	0.20 mm	$t_{rib,anode}$	1.50 mm
$t_{GDL,cathode}$	0.20 mm	$k_{BP,thr}$	20 W m^{-1} K^{-1}
t_{CCM}	0.05 mm	$k_{BP,in}$	60 W m^{-1} K^{-1}
l_{cell}	280.0 mm	$k_{GDL,in}$	10 W m^{-1} K^{-1}
$w_{cell} = l_{ch}$	60.00 mm	$k_{GDL,thr}$	0.7 W m^{-1} K^{-1}
$h_{ch,cathode}$	2.50 mm	k_{CCM}	1.5 W m^{-1} K^{-1}
$h_{ch,anode}$	1.50 mm	k_{H_2}	0.18 W m^{-1} K^{-1}
$w_{ch,cathode}$[a]	2.50 mm	D	From Eq. (9)
$w_{ch,anode}$[a]	1.00 mm	V_{cell}	From experiment
$\theta_{ch,cathode}$	80°	I	From experiment
$\theta_{ch,anode}$	80°	E	1.253 V

a In trapezoidal cross-section, w is the longer side.

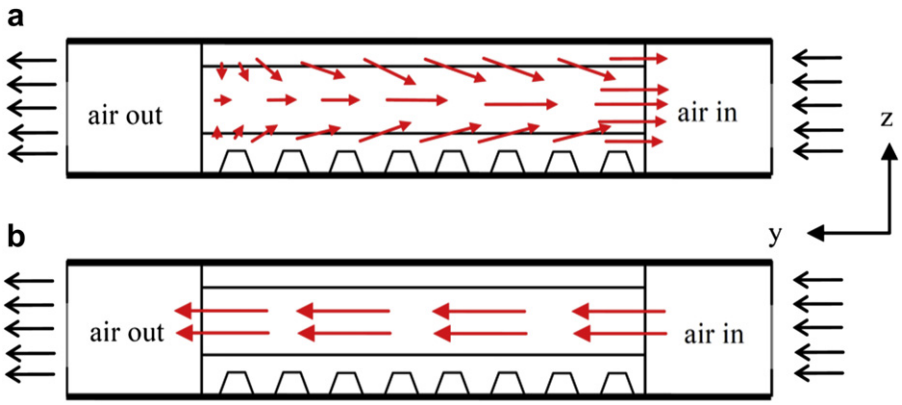

Fig. 6 – Schematic of heat flux vectors: (a) conductive heat flux; and (b) convective heat flux.

Two major modes of heat transfer in air-cooled fuel cells are forced convective heat transfer in cathode channels and conductive heat transfer in the entire domain. The direction of the convective heat flux is the same as the flow direction whereas the direction of the conductive heat flux is determined by the temperature gradient which is in the opposite direction of the flow, as schematically shown in Fig. 6. Interestingly, the combined heat transfer mechanism exhibits completely three-dimensional characteristics, thereby justifying the proposed use of a three-dimensional numerical modeling approach.

Fig. 7 compares the absolute values of the local convective and conductive heat fluxes along the channel. The convective heat flux is calculated as follows:

$$q''_{conv} = \frac{\dot{m}_{air} c_p \frac{dT_m}{dy}}{\Gamma} \tag{12}$$

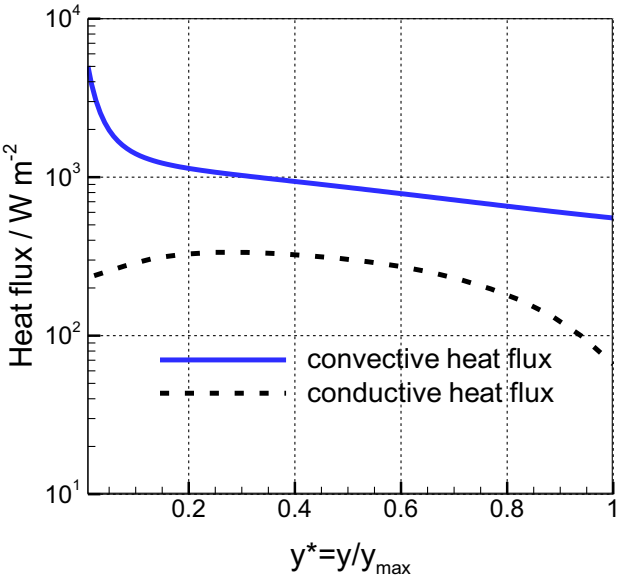

Fig. 7 – Absolute values of mean conductive and convective heat flux in the direction of air flow (reference case).

where T_m is the velocity-weighted average of the temperature distribution over the cross-section and Γ is the channel perimeter. The convective heat flux is based on the channel wall area while the conductive heat flux calculated from Eq. (13) is based on the domain cross-sectional area.

$$q''_{cond} = \frac{1}{A_c} \int_{A_c} -k \frac{\partial T}{\partial y} \, dA_c \tag{13}$$

Therefore, to compare the order of magnitude of these two heat fluxes in Fig. 7, q''_{cond} in Eq. (13) is multiplied by a factor of A_c/A_w, where A_c is the domain cross-sectional area and A_w is the channel wall surface area. Note that the conductive heat flux is negative in the air flow direction. As can be inferred from Fig. 7, at the inlet, the convective heat flux is one order of magnitude higher than the conductive heat flux. Moreover, the convective heat flux has its maximum at the inlet and decreases in the flow direction consistently while the conductive heat flux has its maximum value internally at some point after the inlet. This is due to the different variation of the fluid bulk temperature and the plate temperature gradient in the flow developing region.

In Table 3, the values of total convective and conductive heat transfer dissipated from the domain to the surroundings are calculated by integrating Eq. (12) over the channel wall area and Eq. (13) over the inlet and outlet cross-sectional area of the domain respectively. Also, the percentages of each type of heat transfer, under different conditions (air velocity and plate thermal conductivity), are compared in Table 3. At high air velocities, convection is the major part of heat transfer, and the contribution of conductive heat transfer becomes more important as the plate thermal conductivity increases. In general, the convective heat dissipation is an order of magnitude (~10×) higher than the conductive portion.

Simulations of the water vapor distribution are also conducted for the reference case air-cooled fuel cell configuration. The resulting variation of the average relative humidity and water vapor mass fraction inside the cathode channel is plotted in Fig. 8. As a result of the water generation in the cathode catalyst layer (calculated using Eq. (10)) and associated mass flux into the relatively dry cathode air channel, the mass fraction of water vapor increases along the channel. Although a significant amount of water vapor diffuses into the

Table 3 – Comparison of simulated conductive and convective heat dissipation to the surroundings.

Case#	Air velocity u [m s^{-1}]	Plate thermal conductivity k_{BP} [W m^{-1} K^{-1}]	Convective heat transfer $\dot{Q}_{conv}$ [W]	Conductive heat transfer $\dot{Q}_{cond}$ [W]	Percentage of convective heat transfer	Percentage of conductive heat transfer
1	4.0	30	0.289	0.011	96%	4%
2	3.0	50	0.27	0.03	90%	10%
3	2.0	30	0.264	0.036	88%	12%
4	4.0	60	0.262	0.038	87%	13%

All parameters are kept constant in different cases except the oxidant flow rate and plate thermal conductivity.

channel, it is noteworthy to observe that the average relative humidity is decreasing from 25% at the inlet to 11% at the outlet of the cathode channel. This is due to the temperature rise in the air flow, which increases the saturation pressure and controls the relative humidity. It is therefore important to consider the coupled effects of humidity and temperature in air-cooled fuel cells.

3.3. *Parametric study*

In this section, the effects of selected parameters such as air inlet velocity, bipolar plate thermal conductivity, and GDL thermal conductivity on the maximum temperature and temperature distribution in the fuel cell stack are investigated. In the parametric studies, only one parameter is varied while all other inputs parameters are kept the same as the reference case (see Table 2). The air velocities and plate thermal conductivities considered here are based on a practical range of fan operating conditions and graphite based bipolar plate materials, respectively. For the range of bipolar plate thermal conductivity see Refs. [32] and [33].

The results of varying the air velocity and bipolar plate thermal conductivity are plotted in Figs. 9 and 10, respectively. By increasing the air inlet velocity, the maximum stack temperature drops considerably, as expected. Increasing the bipolar plate thermal conductivity also has a positive impact on reducing the temperature in the entire domain, although not as significantly as for air velocity. Both air velocity and plate thermal conductivity are thus important parameters for thermal management of air-cooled stacks. There are highly thermally conductive materials such as pyrolytic graphite sheet (with thermal conductivity of 600–800 W m^{-1} K^{-1} in the in-plane directions) that can be used for efficient heat transfer in the stack [32].

Fig. 11 shows the effect of the GDL thermal conductivity on temperature distribution along the channel (see Ref. [34] for the GDL effective thermal conductivity range). It can be observed that unlike the bipolar plate thermal conductivity, which has significant impact on the overall heat transfer characteristics, changing the GDL thermal conductivity does not alter the temperature distribution, at least within the studied range. This is due to the fact that both thickness and thermal conductivity of bipolar plate are one order of magnitude higher than that of GDL. The effect of anisotropic GDL thermal conductivity is also analyzed in Fig. 11: in-plane and through-plane thermal conductivities of 17 and 0.5 W m^{-1} K^{-1} respectively are compared to the isotropic case of 0.5 W m^{-1} K^{-1} (see Ref. [35] for the GDL in-plane thermal conductivity). According to our modeling results, the GDL thermal conductivity does not change the temperature profiles significantly in any of the cases studied. Because of

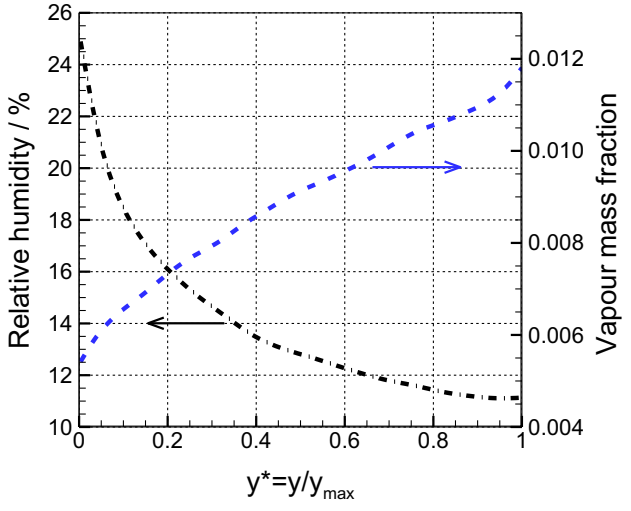

Fig. 8 – Relative humidity and water vapor mass fraction along the cathode channel.

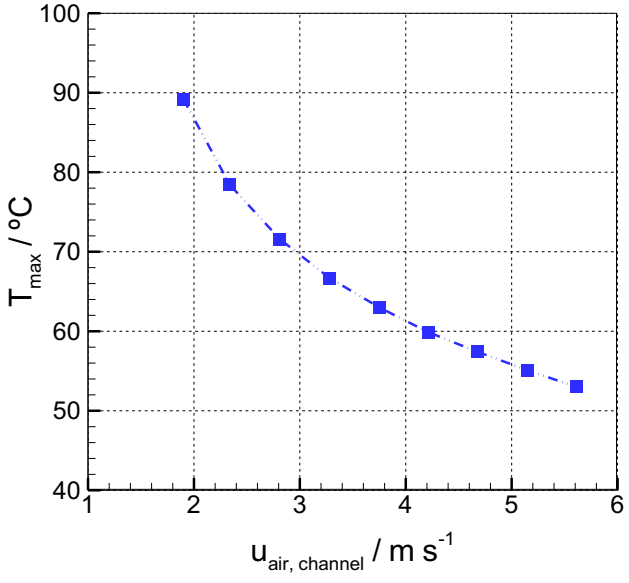

Fig. 9 – Effect of air velocity on maximum stack temperature.

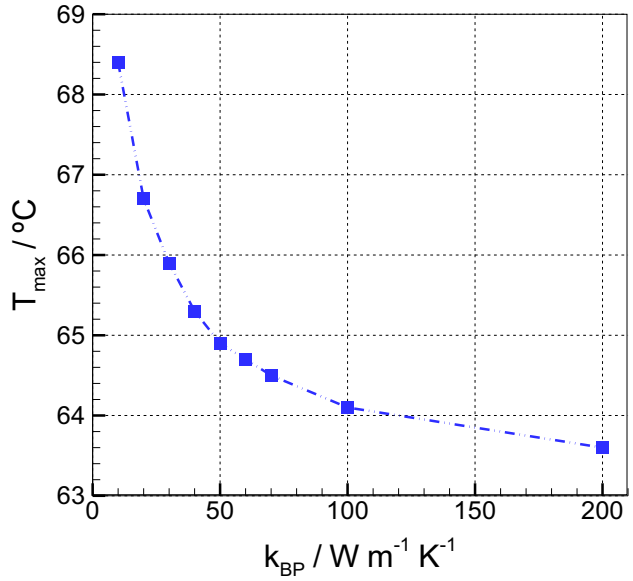

Fig. 10 – Effect of bipolar plate thermal conductivity on maximum stack temperature.

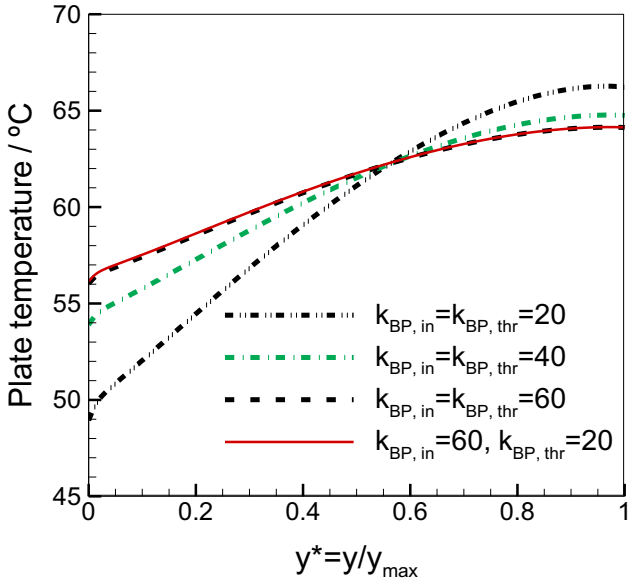

Fig. 12 – Effect of bipolar plate in-plane and through-plane thermal conductivity on plate temperature distribution along the channel. Unit of thermal conductivity is [W m^{-1} K^{-1}].

the high air flow rate, the heat transfer in air-cooled fuel cells is primarily controlled by convection and thus GDL thermal conductivity does not play a major role.

Similarly, the effect of isotropic and anisotropic bipolar plate thermal conductivity is investigated and the corresponding temperature distributions are plotted in Fig. 12. These results show that the impact of in-plane thermal conductivity of bipolar plate on the temperature distribution is much more significant than the effect of through-plane thermal conductivity. As Fig. 12 shows, higher in-plane thermal conductivity for bipolar plate leads to a more uniform temperature distribution as well as a reduced maximum stack temperature (as discussed previously).

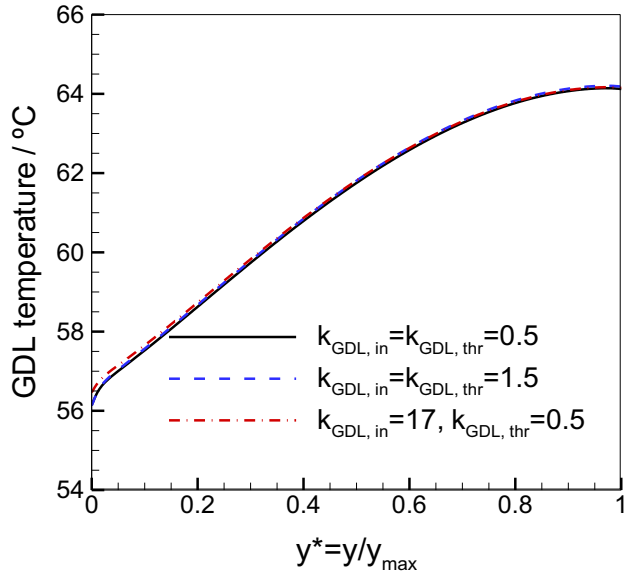

Fig. 11 – Effect of GDL in-plane and through-plane thermal conductivity on GDL temperature distribution along the channel. Unit of thermal conductivity is [W m^{-1} K^{-1}].

4. Conclusions

In the present work, a three-dimensional thermal model is developed to predict the temperature distribution in a PEMFC. The proposed model can be used for design and optimization of cooling devices for PEMFC systems, and is demonstrated here for an air-cooled fuel cell stack. The model is employed to simulate the 3D temperature profiles and estimate the maximum temperature in an air-cooled PEMFC stack, without considering the entire stack as the solution domain. The validity of the model is verified by comparison of the numerical results with experimental data for Ballard Power Systems' air-cooled ACS stack, which shows a good agreement for a wide range of conditions. The slight difference is likely due to the uncertainty in material properties and air velocity measurement.

The validated model is utilized to analyze and compare the different heat transfer regimes, revealing that in air-cooled fuel cell stacks, where the air stoichiometry is high, the contribution of the forced convection heat transfer to the total heat rejection is much higher than thermal conduction. In fact, our parametric studies show that the air velocity and bipolar plate in-plane thermal conductivity are two critical factors that affect the temperature distribution in an air-cooled fuel cell and thus play an important role in thermal management of the stack. Moreover, according to our parametric studies, the GDL thermal conductivity does not change the temperature of the air-cooled fuel cell significantly. This conclusion is specific to the fuel cell stacks in

which convective heat transfer is considerably higher than conductive heat transfer. It is also determined that humidity and temperature distributions are highly coupled in air-cooled cells. Despite water generation in the cell, the relative humidity may decrease along the channel due to the rising temperature towards the outlet.

In our future work, the present thermal model will be integrated with a performance model in order to investigate the effects of parameters that influence the fuel cell current and voltage and provide a more detailed analysis of the heat generation in the stack. This three-dimensional model for single cells will form a theoretical foundation for thermal analysis of multi-cell stacks where thermal management and stack cooling is a significant engineering challenge.

Acknowledgments

Funding for this research provided by Ballard Power Systems, Inc., Natural Sciences and Engineering Research Council of Canada, Western Economic Diversification Canada, Canada Foundation for Innovation, British Columbia Knowledge Development Fund, and Simon Fraser University is highly appreciated. We also gratefully acknowledge the in-kind contributions provided by Ballard Power Systems and the support from the following individuals: Julie Bellerive, David Harvey, and Shanna Knights.

Nomenclature

A_c	cross-sectional area of the channel, m^2
A_w	surface area of the channel walls, m^2
c	concentration, mol m^{-3}
c_p	specific heat, J K^{-1} kg^{-1}
D	diffusion coefficient, m^2 s^{-1}
E	thermal voltage, V
F	Faraday's constant, C mol^{-1}
H	enthalpy, J
I	electrical current, A
k	thermal conductivity, W m^{-1} K^{-1}
l	length, m
M	molar mass, g mol^{-1}
$\dot{m}$	mass flow rate, kg s^{-1}
n_{cell}	number of cells in a stack, –
n	number of moles of electrons per mole of reactant, –
$\mathbf{n}$	outward unit normal, –
p	pressure, Pa
PEM	polymer electrolyte membrane
$\dot{q}$	heat generation per unit volume, W m^{-3}
q''	heat generation per unit area, W m^{-2}
$\dot{Q}$	total heat generation, W
S_{mass}	mass source term, kg m^{-3} s^{-1}
T	temperature, K
t	thickness, m
u	velocity, m s^{-1}
$\mathbf{u}$	velocity vector, m s^{-1}
V	output voltage, V
$\dot{W}$	power, W
w	width, m; water vapor mass fraction, –

Greek symbols

Γ	channel perimeter, m
θ	smaller angle in trapezoidal cross-section
μ	fluid viscosity, N s m^{-2}
ρ	density, kg m^{-3}

Subscripts

atm	atmospheric
BP	bipolar plate
CCM	catalyst coated membrane
cell	single fuel cell
ch	channel
cond	conduction
conv	convection
exp	experiment
f	fluid
GDL	gas diffusion layer
in	inlet, in-plane
m	mean
MEA	membrane electrode assembly
out	outlet
sim	simulation
thr	through-plane

REFERENCES

[1] Mench MM. In: Fuel cell engines. 1st ed. New Jersey: John Wiley & Sons; 2008.
[2] Larminie J, Dicks A. In: Fuel cell systems explained. 2nd ed. Chichester: John Wiley & Sons; 2003.
[3] Faghri A, Guo Z. Challenges and opportunities of thermal management issues related to fuel cell technology and modeling. International Journal of Heat and Mass Transfer 2005;48:3891–920.
[4] van den Oosterkamp PF. Critical issues in heat transfer for fuel cell systems. Energy Conversion and Management 2006; 47:3552–61.
[5] Berning T, Djilali N. Three-dimensional computational analysis of transport phenomena in a PEM fuel cell – a parametric study. Journal of Power Sources 2003;124: 440–52.
[6] Wang L, Husar A, Zhou T, Liu H. A parametric study of PEM fuel cell performances. International Journal of Hydrogen Energy 2003;28:1263–72.
[7] Gasteiger HA, Panels JE, Yan SG. Dependence of PEM fuel cell performance on catalyst loading. Journal of Power Sources 2004;127:162–71.
[8] Pathapati PR, Xue X, Tang J. A new dynamic model for predicting transient phenomena in a PEM fuel cell system. Renewable Energy 2005;30:1–22.
[9] Ferng YM, Tzang YC, Pei BS, Sun CC, Su A. Analytical and experimental investigations of a proton exchange membrane fuel cell. International Journal of Hydrogen Energy 2004;29: 381–91.
[10] Schwarz DH, Djilali N. 3D modeling of catalyst layers in PEM fuel cells. Journal of The Electrochemical Society 2007;154: B1167–78.
[11] Inoue G, Yoshimoto T, Matsukuma Y, Minemoto M, Itoh H, Tsurumaki S. Numerical analysis of relative humidity distribution in polymer electrolyte fuel cell stack including cooling water. Journal of Power Sources 2006;162:81–93.

[12] Huisseune H, Willockx A, De Paepe M. Semi-empirical along-the-channel model for a proton exchange membrane fuel cell. International Journal of Hydrogen Energy 2008;33:6270–80.
[13] Inoue G, Yoshimoto T, Matsukuma Y, Minemoto M, Itoh H, Tsurumaki S. Effect of flow pattern of gas and cooling water on relative humidity distribution in polymer electrolyte fuel cell. Journal of Power Sources 2006;162:94–104.
[14] Scholta J, Haussler F, Zhang W, Kuppers L, Jorissen L, Lehnert W. Development of a stack having an optimized flow field structure with low cross transport effects. Journal of Power Sources 2006;155:60–5.
[15] Chang PAC, St-Pierre J, Stumper Jr , Wetton B. Flow distribution in proton exchange membrane fuel cell stacks. Journal of Power Sources 2006;162:340–55.
[16] Liu Z, Mao Z, Wang C, Zhuge W, Zhang Y. Numerical simulation of a mini PEMFC stack. Journal of Power Sources 2006;160:1111–21.
[17] Shimpalee S, Dutta S. Numerical prediction of temperature distribution in PEM fuel cells. Numerical Heat Transfer Part A 2000;38:111–28.
[18] Fuller TF, Newman J. Water and thermal management in solid-polymer-electrolyte fuel cells. Journal of The Electrochemical Society 1993;140:1218–25.
[19] Ju H, Meng H, Wang CY. A single-phase, non-isothermal model for PEM fuel cells. International Journal of Heat and Mass Transfer 2005;48:1303–15.
[20] Chupin S, Colinart T, Didierjean S, Dubé Y, Agbossou K, Maranzana G, et al. Numerical investigation of the impact of gas and cooling flow configurations on current and water distributions in a polymer membrane fuel cell through a pseudo-two-dimensional diphasic model. Journal of Power Sources 2010;195:5213–27.
[21] Promislow K, Wetton B. A simple, mathematical model of thermal coupling in fuel cell stacks. Journal of Power Sources 2005;150:129–35.
[22] Shan Y, Choe SY. A high dynamic PEM fuel cell model with temperature effects. Journal of Power Sources 2005;145:30–9.
[23] Yu S, Jung D. Thermal management strategy for a proton exchange membrane fuel cell system with a large active cell area. Renewable Energy 2008;33:2540–8.
[24] Pharoah JG, Burheim OS. On the temperature distribution in polymer electrolyte fuel cells. Journal of Power Sources 2010;195:5235–45.
[25] Adzakpa KP, Ramousse J, Dubé Y, Akremi H, Agbossou K, Dostie M, et al. Transient air cooling thermal modeling of a PEM fuel cell. Journal of Power Sources 2008;179:164–76.
[26] Sinha PK, Wang CY, Beuscher U. Transport phenomena in elevated temperature PEM fuel cells. Journal of the Electrochemical Society 2007;154:B106–16.
[27] Sasmito AP, Lum KW, Birgersson E, Mujumdar AS. Computational study of forced air-convection in open-cathode polymer electrolyte fuel cell stacks. Journal of Power Sources 2010;195:5550–63.
[28] Ramousse J, Adzakpa KP, Dube Y, Agbossou K, Fournier M, Poulin A, et al. Local voltage degradations (drying and flooding) analysis through 3D stack thermal modeling. Journal of Fuel Cell Science and Technology 2010;7:041006–10.
[29] Musio F, Tacchi F, Omati L, Gallo Stampino P, Dotelli G, Limonta S, et al. PEMFC system simulation in MATLAB-Simulink® environment. International Journal of Hydrogen Energy 2011;36:8045–52.
[30] Djilali N. Computational modelling of polymer electrolyte membrane (PEM) fuel cells: challenges and opportunities. Energy 2007;32:269–80.
[31] Bolz R, Tuve G. In: Handbook of tables for applied engineering science. 2nd ed. Cleveland: CRC Press; 1976.
[32] Wen C-Y, Huang G-W. Application of a thermally conductive pyrolytic graphite sheet to thermal management of a PEM fuel cell. Journal of Power Sources 2008;178:132–40.
[33] Du L. Highly conductive epoxy/graphite polymer composite bipolar plates in proton exchange membrane (PEM) fuel cells. Akron, Ohio: The University of Akron; 2008.
[34] Sadeghi E, Djilali N, Bahrami M. Effective thermal conductivity and thermal contact resistance of gas diffusion layers in proton exchange membrane fuel cells. Part 1: effect of compressive load. Journal of Power Sources 2011;196:246–54.
[35] Sadeghi E, Djilali N, Bahrami M. A novel approach to determine the in-plane thermal conductivity of gas diffusion layers in proton exchange membrane fuel cells. Journal of Power Sources 2011;196:3565–71.